Progress In Electromagnetics Research C, Vol. 153, 71–80, 2025

PIER C

(Received 30 November 2024, Accepted 24 January 2025, Scheduled 28 February 2025)

Magnetic Resonance Eddy Current Testing Based on Deep Learning Axis Identification and Reconstruction of Reinforced Concrete Penetration Image

Zhengxuan Zhang[1], Jingming Zhang[2], and Leng Liao[2, *]

[1] *School of Information Science and Engineering, Chongqing Jiaotong University, Chongqing 400074, China*
[2] *School of Materials Science and Engineering, Chongqing Jiaotong University, Chongqing 400074, China*

ABSTRACT: Accurately identifying and calibrating reinforcement bars in concrete is a significant challenge due to their invisibility. This paper proposes a deep learning-based method using magnetic resonance eddy penetrating imaging (MREPI) to acquire data on steel bars embedded in concrete. The data is processed into images and input into the Skel-Unet neural network to extract angle and position information of the central axis of the steel bars. Based on this information, the steel bar diameters are determined. A novel image reconstruction method is also introduced to integrate rebar dimension variations for precise calibration. Experimental results show that the Skel-Unet model achieves high accuracy, with training and testing loss values below 0.01, and F1 score reaches 0.7436. The reconstructed images clearly delineate the position, dimensions, and orientation of the rebars, enhancing calibration and nondestructive testing in structural health monitoring.

1. INTRODUCTION

Reinforced concrete is widely used in buildings [1], and detecting and identifying steel bar sizes during construction and maintenance is often necessary [2]. However, detecting and imaging the inner reinforcement is challenging due to the concrete covering, making conventional methods ineffective [3]. As a result, imaging and detection of reinforced concrete has become a research focus in recent years.

Current methods for rebar penetration imaging in concrete include ultrasonic scanning [4, 5], infrared thermal imaging [6, 7], nuclear magnetic resonance (NMR) spectroscopy [8], and eddy current detection [9]. Ultrasonic scanning detects rebar location by measuring echo signal changes, but its effectiveness is limited by rapid wave decay and concrete uniformity. Infrared thermal imaging detects surface temperature distribution to identify reinforcement location and damage, but its depth is limited and affected by ambient temperature and surface conditions [10]. NMR provides high-quality internal structure images but requires expensive equipment and complex operation.

The eddy current testing method has low cost, is minimally affected by ambient temperature and concrete uniformity, and excels in detecting and imaging reinforcement in concrete. In 2007, Rubinacci et al. [9] developed a finite element model based on eddy current testing (ECT) principles to locate and identify the size of steel bars in concrete. Kasai et al. [11] proposed an eddy current sensor with a copper core induction, verifying its effectiveness in detecting defects in aluminum plates through finite element analysis and experiments. Chen et al. [12] applied a magnetic resonance eddy current sensor with double coils for reinforced concrete penetration imaging, successfully distinguishing reinforcement and rust within the concrete.

Although manual or statistical methods can determine the diameter of steel bars in inspection data, these approaches depend on prior knowledge and operator experience. To improve accuracy, machine learning techniques are essential. Recent research has applied machine learning in reinforced concrete inspection. Li et al. [13] used the Yolo v3 real-time target detection algorithm for the automatic identification of rebar signals in ground penetrating radar images, employing a one-dimensional convolutional neural network to identify rebar diameter and concrete cover thickness. Feng et al. [14] enhanced crack identification in bridge concrete using a deep convolutional neural network-based image super-resolution algorithm, improving accuracy by 16%. Wang et al. [15] proposed an optimized Residual Channel Attention Network to reduce reinforcement clutter in concrete defect detection. Jeon et al. [16] used deep learning-based electrical resistance tomography for precise rebar position detection, achieving 95.6% accuracy. Wang et al. [17] tackled rebar clutter suppression in ground penetrating radar by using unsupervised learning to reconstruct defect signals while suppressing rebar signals.

Existing methods for detecting rebar defects, size, and concrete cover often lack the visualization of internal reinforcement. This study proposes a deep learning approach using magnetic resonance eddy current imaging to extract rebar axial images and determine size through peak and valley voltage discrimination. The method collects and normalizes detection

---

* Corresponding author: Leng Liao (lengliao@cqjtu.edu.cn).

doi:10.2528/PIERC24113002

Published by THE ELECTROMAGNETIC ACADEMY

data, applies Skel-Unet for axis extraction, and uses the Canny-lines algorithm to detect slopes for voltage-based size analysis. Finally, size information is visualized, showing rebar direction and dimensions within concrete.

2. PREVIOUS WORK

The magnetic resonance eddy current penetration imaging sensor used in magnetic resonance penetration detection is shown in Figure 1. The excitation coil and resonant coil are coaxially wound around a ferrite, concentrating the magnetic flux at the center of each coil. Chen et al. [12] used this sensor for preliminary steel bar detection experiments.

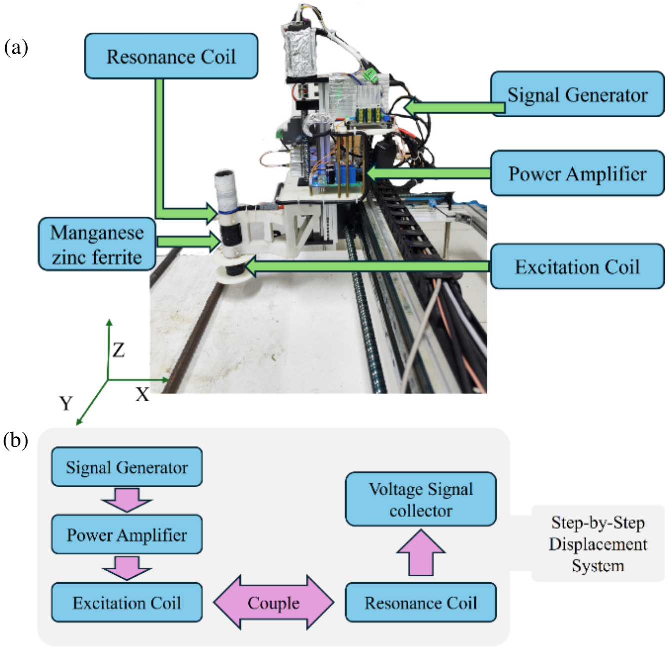

FIGURE 1. *XYZ* triaxial scanning system and magnetic resonance eddy current sensor.

The magnetic resonance eddy current sensor effectively detects reinforcement within concrete and enables penetrating imaging. Using this sensor, an *XYZ* three-axis scanning system is built to conduct experiments on steel bar penetration imaging and size identification.

3. DATA COLLECTION

3.1. Imaging Data Acquisition of Rebar Penetration Based on Magnetic Resonance Sensor

Using a magnetic resonance eddy current penetration imaging sensor, the probe moves through the steel bar's spontaneous leakage magnetic field. As the sensor approaches the steel bar, the voltage decreases; as it moves away, the voltage increases. To collect data, a 90 mm × 90 mm square area centered on the steel bar is gridded into 19×19 points with 5 mm spacing. Each point represents a data collection site, requiring 5 seconds to stabilize. This setup balances the need for data density and reasonable acquisition time. Figure 2 illustrates this process, with blue circles for the probe position, gray for collected points, white for uncollected points, an arrow for movement, and orange for the steel bar.

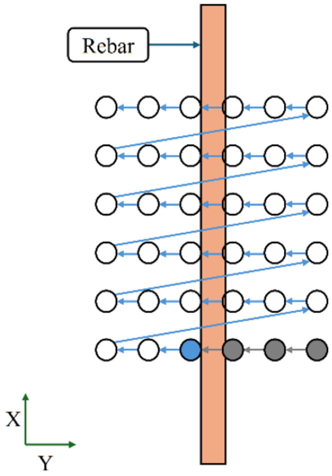

FIGURE 2. Schematic diagram for voltage matrix acquisition.

After acquiring the voltage matrix, the voltage matrix can be normalized to transform it into an image. Taking the pixel value range of 0–255 as an instance, the normalization formula is presented as follows:

$$x_{\text{value}}^{\text{mid}} = 255 \cdot \left(\frac{x - x_{\min}}{x_{\max} - x_{\min}} \right) \tag{1}$$

$$x_{\text{value}}^{\text{final}} = 255 - x_{\text{value}}^{\text{mid}} \tag{2}$$

Figure 4 shows some of the steel bars and reinforced concrete specimens used for data collection. As penetration imaging results for bare reinforcement and reinforced concrete (Figure 3) are consistent across diameters, concrete does not affect imaging. Thus, both specimen types are used to ensure sufficient data. Meanwhile, the thickness of the protective layer in reinforced concrete is shown in Figure 5.

3.2. Judgment of Steel Bar Diameter Based on Peak-Valley Voltage Value

Although normalized steel bar penetration imaging cannot distinguish dimensions, plotting single-line voltage data (Figure 6) reveals a trough where voltage decreases as the sensor approaches the steel bar and increases as it moves away. The red dot marks the minimum voltage, recorded when the sensor is directly above the steel bar. At a 45 mm height, experiments show a linear decrease in minimum voltage with increasing steel bar diameter (Figure 7), indicating a linear relationship between diameter and voltage. Thus, a peak-valley voltage method is proposed to determine steel bar diameters, as shown in Table 1.

Manually calibrating the direction and position of steel bars within concrete is time-consuming. To improve efficiency, a method is proposed to extract the rebar's central axis using Skel-Unet, determining position, slope, and size based on peak-valley voltage data. Using Table 1, a correlation table of size, voltage, and reconstruction coefficients is established (Table 5), enabling reconstruction of penetration images that include size and direction. This enhances calibration efficiency and visu-

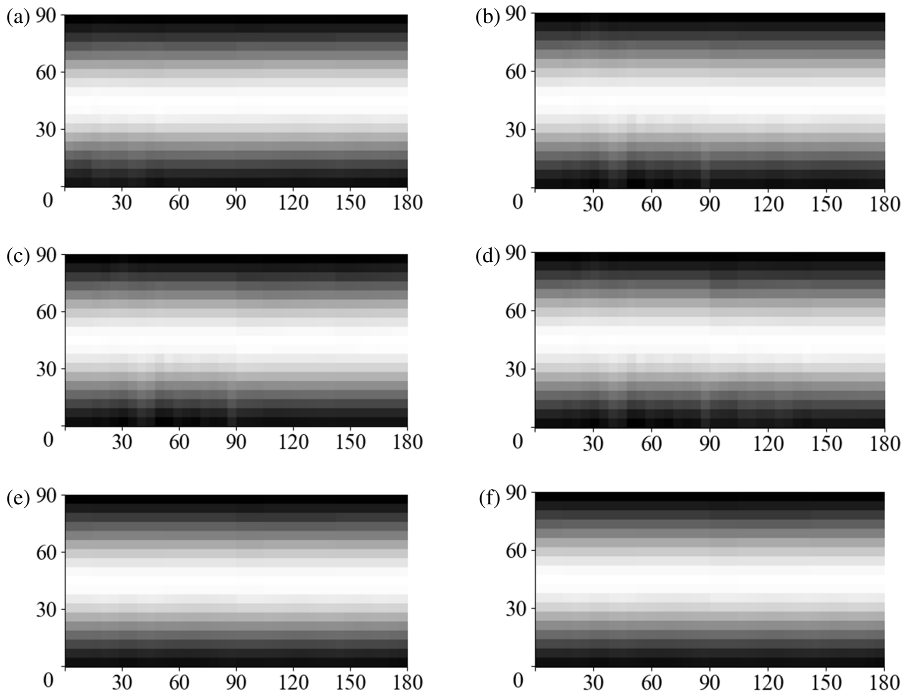

FIGURE 3. Scanning results of bare steel bars and reinforced concrete specimens of various diameters (unit: mm), (a) 20 mm reinforced concrete specimen, (b) 18 mm reinforced concrete specimen, (c) 16 mm reinforced concrete specimen, (d) 14 mm reinforced concrete specimen, (e) 12 mm reinforced concrete specimen, (f) 10 mm reinforced concrete specimen.

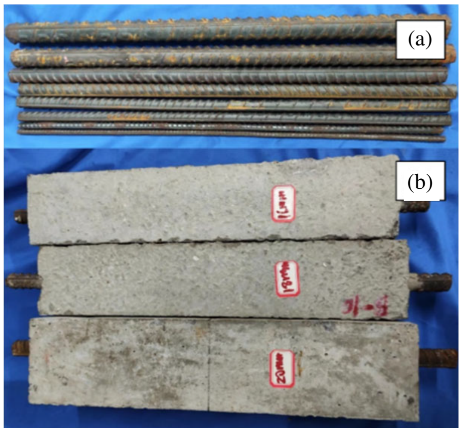

FIGURE 4. Part of the steel bar and concrete samples tested, (a) steel bar, (b) concrete.

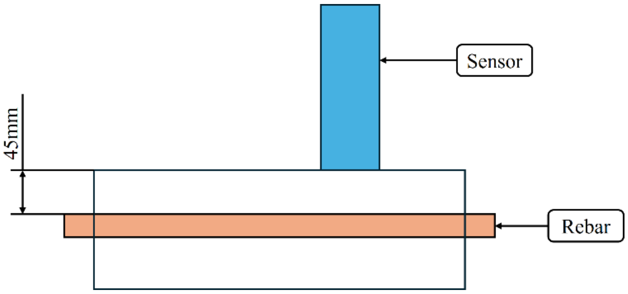

FIGURE 5. Thickness of protective layer in reinforced concrete.

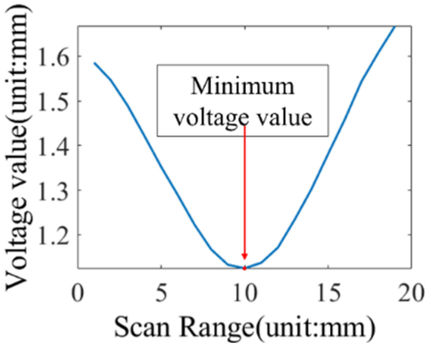

FIGURE 6. Single line voltage value change curve (unit: mm).

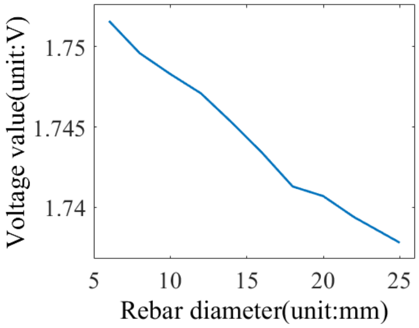

FIGURE 7. Variation curve of steel bar diameter and voltage (unit: mm).

TABLE 1. Diameter and voltage mapping table (unit: mm).

Diameter	6	8	10	12	14	16	18	20	22	25
Voltage	1.7516	1.7496	1.7483	1.7471	1.7453	1.7434	1.7413	1.7407	1.7394	1.7378

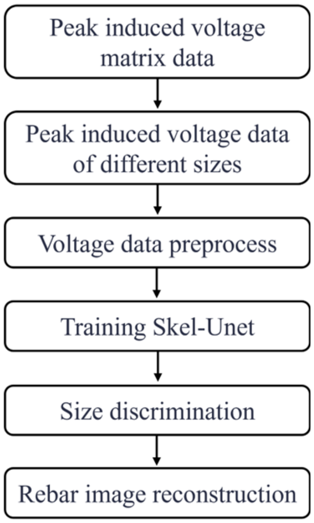

FIGURE 8. Flowchart of magnetic resonance reinforcement detection and image reconstruction.

alizes internal steel bars. Figure 8 shows the flowchart of this method.

3.3. Dataset Construction

Deep learning requires substantial data; hence, 150 samples per size were tested for 10 steel bar sizes (6–25 mm), totaling 1542 vertical rebar images, including vertical, 45° diagonal, and horizontal orientations. Due to poor performance of traditional methods, the Skel-Unet network [18] was used to skeletonize rebar images, requiring labeled datasets with annotated centerlines. The prepared dataset supports the extraction of rebar central axes and the development of advanced image processing techniques. The next section details using Skel-Unet for central axis extraction and rebar image reconstruction.

4. REBAR CENTRAL AXIS EXTRACTION AND IMAGE RECONSTRUCTION

4.1. Algorithm

4.1.1. Network Architecture of Skeletonization Unet

Skeletonization Unet, proposed by Nguyen [18], extends Unet (Olaf Ronneberger, 2015) [26] for skeleton extraction by incorporating attention mechanisms in the encoder and convolutional block attention module (CBAM) modules in the decoder. This adaptation enables Unet to extract the central axis of inclined steel bars. Figure 9, which corresponds to Figure 1 in [18], shows the structure of Skeletonization Unet.

Similar to classic Unet, the network comprises encoder and decoder sections. As shown in Figure 11, use both 3×3 convolution kernels, with 2×2 kernels for pooling in the encoder and upsampling in the decoder. To enhance skeleton extraction, the encoder incorporates a multi-head attention module [20] with a Decision branch and a Feature group. The Feature group uses 3×3 convolution for feature extraction, while the Decision branch applies 1×1 convolution and softmax to weight feature maps (Figure 10), as shown in Figure 10, which corresponds to Figure 2 in [18].

The decoder uses 2×2 upsampling and 3×3 convolutions for image reconstruction, with a CBAM [21] added after each 3×3 convolution and before 2×2 upsampling. CBAM combines channel and spatial attention to enhance the weighting of key features, improving skeleton extraction performance, as shown in Figure 11, which corresponds to Figure 3 in [18].

4.1.2. Loss Function

To address the issue of unbalanced classification of networks in skeletonized tasks and evaluate network performance more precisely, Weighted focal loss [22] is employed as shown in Equation (14), which corresponds to Equation (1) in [18]:

$$L_{\text{focal}} = \alpha p^{\gamma} \log(p) + (1-\alpha)(1-p)^{\gamma} \log(1-p) \tag{3}$$

where α represents the weight of the positive class, p the probability that the sample pertains to the positive class, and γ the focusing parameter.

Dice loss [23] is generally used to minimize the overlap of prediction and target in the field of image segmentation, so Dice loss and Weighted focal loss are also added together, as shown in Equations (15) and (16), which corresponds to Equations (2) and (3) in [18]:

$$L_{\text{dice}} = 1 - 2\frac{\sum_i y_i p_i + \epsilon}{\sum_i y_i + \sum_i p_i + \epsilon} \tag{4}$$

$$L = L_{\text{dice}} + L_{\text{focal}} \tag{5}$$

where y_i represents the target label, and ϵ is a constant employed to prevent the denominator from being zero.

Auxiliary task learning [24] shares gradient information across model layers, improving the main task's performance and providing regularization. In Skel-Unet, each decoder layer outputs a predictive image after 1×1 convolution, and its loss is calculated. The final loss is a weighted sum of the losses from all four layers, as shown in Equation (17), which corresponds to Equation (4) in [18]:

$$L_{\text{final}} = 0.5L_{256} + 0.3L_{128} + 0.2L_{64} + 0.1L_{32} \tag{6}$$

where L_{256}, L_{128}, L_{64}, and L_{32} are the loss values of the four layers of the network with different resolutions respectively.

4.1.3. Cannylines Line Detection Algorithm

After Skel-Unet extracts the rebar's central axis, its gradient is calculated to locate peak and valley voltage values in the

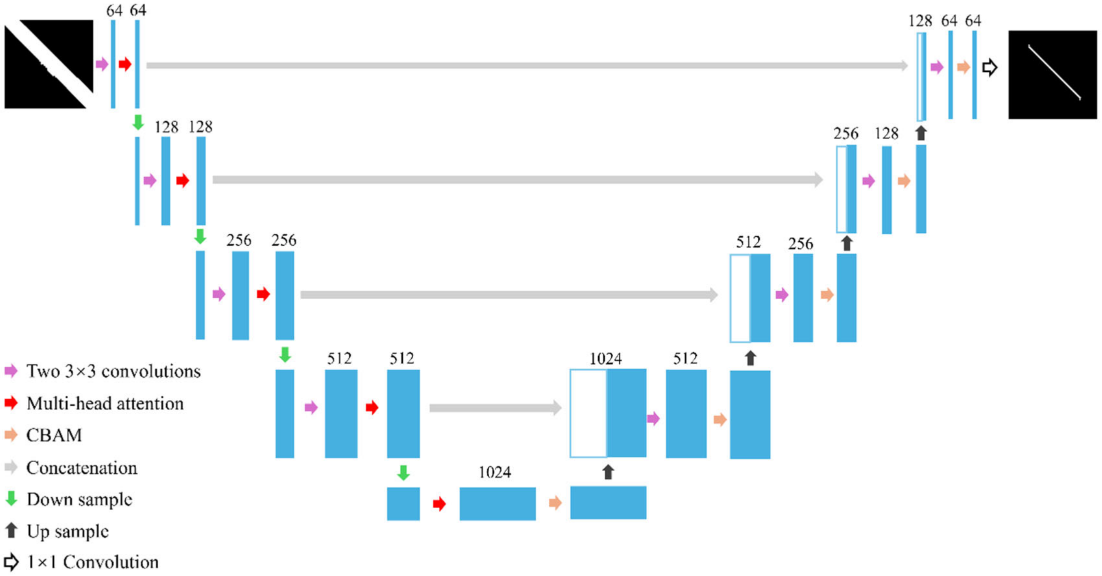

FIGURE 9. The architecture of Skel-Unet.

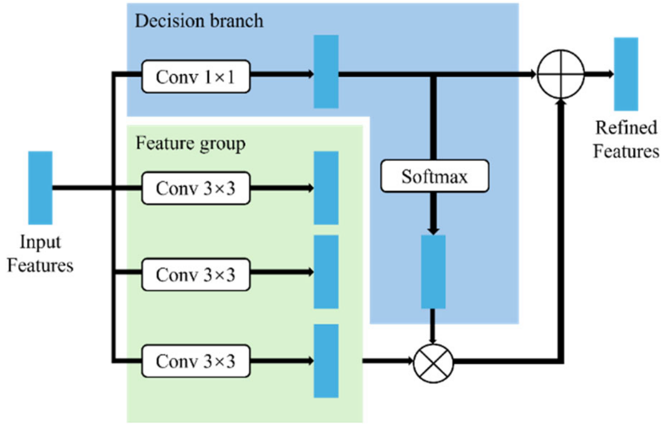

FIGURE 10. Multi-headed attention module.

corresponding matrix for size determination. The Cannylines algorithm [25] uses the Sobel operator to compute the image gradient.

$$G_x = \begin{bmatrix} -1 & 0 & 1 \\ -2 & 0 & 2 \\ -1 & 0 & 1 \end{bmatrix} \otimes I \tag{7}$$

$$G_y = \begin{bmatrix} -1 & -2 & 1 \\ 0 & 0 & 0 \\ 1 & 2 & 1 \end{bmatrix} \otimes I \tag{8}$$

$$G = \sqrt{G_x^2 + G_y^2} \tag{9}$$

$$\theta = \arctan\left(\frac{G_y}{G_x}\right) \tag{10}$$

where G_x and G_y represent the gradients in the vertical and horizontal directions, respectively; I refers to the input image; G denotes the gradient amplitude; and θ indicates the gradient direction. After obtaining the gradient amplitude and direction, the threshold range is determined based on the amplitude.

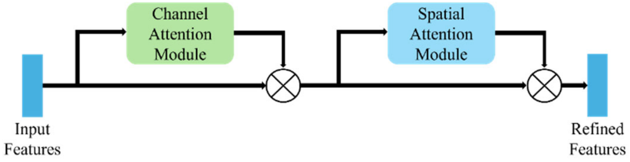

FIGURE 11. Convolutional block attention module.

$$T_H = \text{Percentile}(G, 90) \tag{11}$$

$$T_L = 0.4 \cdot T_H \tag{12}$$

Starting from the edge pixel with the maximum gradient, pixels are collected in both directions of θ to form an initial line segment. Adjacent pixels are checked to see if they should be part of the same line. Lines are separated by calculating the gradient, and if the gradient is below the threshold, and the endpoint is close, the lines are merged. This process identifies the steel bar's central axis.

Once a straight line is detected, the slope of the vertical line can be directly derived from the gradient θ, as there is only one straight line in the steel bar's central axis image.

$$K_{\text{slope}} = -\frac{1}{\tan(\theta)} \tag{13}$$

After determining the slope, a line is drawn through the matrix center in the voltage data, and the peak and valley voltage values are extracted to assess the steel bar's size.

4.2. Network Analysis and Training

In order to measure the model complexity, we count the total number of learnable parameters within each neural network. Table 2 and Table 3 show the number of parameters in Skel-Unet.

TABLE 2. Parameters of each layer in Encoder.

Layer	Conv1+MHA	Conv2+MHA	Conv3+MHA	Conv4+MHA	Conv5+MHA
Params	$(3\times3\times1+1)$ $\times64+(3\times3$ $\times64+1)\times64$	$(3\times3\times64+1)$ $\times128+(3\times3$ $\times128+1)\times128$	$(3\times3\times128+1)$ $\times256+(3\times3$ $\times256+1)\times256$	$(3\times3\times256+1)$ $\times512+(3\times3\times512+1)$ $\times512$	$(3\times3\times512+1)$ $\times1024+(3\times3$ $\times1024+1)\times1024$
Total	37,504	221,440	885,248	2,361,472	14,168,832

TABLE 3. Parameters of each layer in Decoder.

Layer	UpConv1+CBAM	UpConv2+CBAM	UpConv3+CBAM	UpConv4+CBAM
Params	$(2\times2\times1024+1)\times512$ $+(3\times3\times1024+1)\times512$ $+(3\times3\times512+1)\times512$	$(2\times2\times512+1)\times256$ $+(3\times3\times512+1)\times256$ $+(3\times3\times256+1)\times256$	$(2\times2\times256+1)\times128$ $+(3\times3\times256+1)\times128$ $+(3\times3\times128+1)\times128$	$(2\times2\times128+1)\times64$ $+(3\times3\times128+1)\times64$ $+(3\times3\times64+1)\times64$
Total	9,182,336	1,262,208	242,304	87,936

TABLE 4. F1 score of different models.

Model	Unet	ResUnet	Unet++	ResUnet++	Skel-Unet
F1 score	0.2954	0.3451	0.3687	0.5612	0.7436

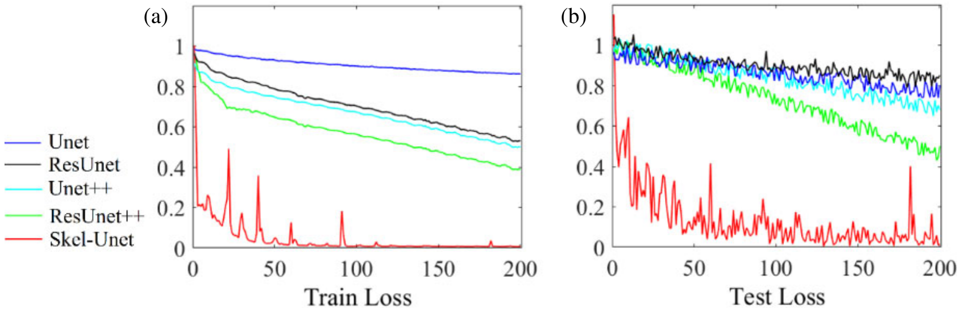

FIGURE 12. Training losses and test losses.

Based on Tables 2 and 3, taking an input size of 256×256 as an example, the model size can be calculated to be 262.55 MB, which allows the model to be deployed on devices with limited memory. Meanwhile, the model's giga floating-point operations per second (GFLOPS) reaches 84.696, which indicates a high demand for computational power. On devices with limited computational resources, this may require more time, making it difficult for the model to complete time-sensitive tasks.

The Skel-Unet was trained and tested on a PC with a Ryzen 7 5800H CPU and RTX 3060 GPU using PaddlePaddle. A self-constructed dataset of vertical, 45° inclined, and horizontal rebars, along with the public Pixel_SkelNet dataset, was used. The learning rate was set to 2×10^{-3}, with 200 iterations and a batch size of 4, to accommodate the 6 GB GPU memory. Due to the recent introduction of U-Net-based models applied in various fields, a comparison with some classic U-Net-based models is conducted. The result is shown in Figure 12.

The prediction results of different models are shown in Figure 13.

To further assess the performance differences among the models, the recorded F1 scores are shown in Table 4.

Skel-Unet effectively extracts the central axis of diagonal reinforcement, while other models fail to do so. The extracted central axes of rebar from different angles using Skel-Unet are shown in Figure 14.

4.3. Rebar Image Reconstruction

By combining voltage size discrimination with imaging, the diameter, position, and direction of the rebar are integrated into the image, improving the efficiency of collection, calibration, and discrimination. A corresponding table of voltage, diameter, and pretreatment coefficient is shown in Table 5.

Once the table is established, bilinear interpolation is used to resize the image to 256×256, allowing for better observation and accurate incorporation of diameter information. The bilinear interpolation algorithm [19] is as follows:

$$f(x,y_1) = \frac{x_2-x}{x_2-x_1}f(Q_{11})+\frac{x-x_1}{x_2-x_1}f(Q_{21}) \quad (14)$$

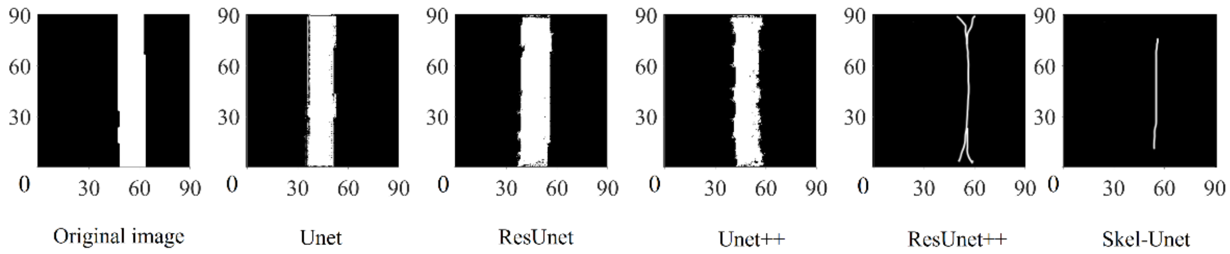

FIGURE 13. Comparison of skeleton extraction via different models (unit: mm).

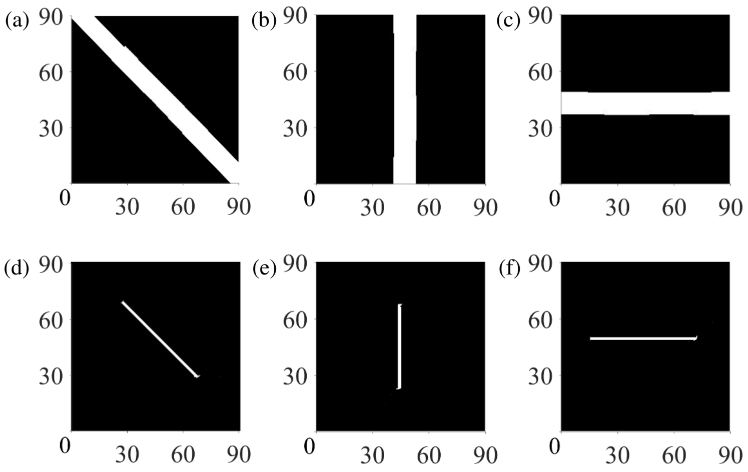

FIGURE 14. Images of central axes in different angles (unit: mm), (a) diagonal 45° bar; (b) vertical bar; (c) horizontal bar.

TABLE 5. Voltage, diameter and coefficient mapping table.

Diameter (mm)	6	8	10	12	14	16	18	20	22	25
Voltage (V)	1.7516	1.7496	1.7483	1.7471	1.7453	1.7434	1.7413	1.7407	1.7394	1.7378
Coefficient	8.5	6.8	5.4	4.4	3.5	2.8	2.2	1.7	1.4	1

$$f(x, y_2) = \frac{x_2 - x}{x_2 - x_1} f(Q_{12}) + \frac{x - x_1}{x_2 - x_1} f(Q_{22}) \quad (15)$$

$$f(x, y) = \frac{y_2 - y}{y_2 - y_1} f(x, y_1) + \frac{y - y_1}{y_2 - y_1} f(x, y_2) \quad (16)$$

The variables in the formula are shown in Figure 15.

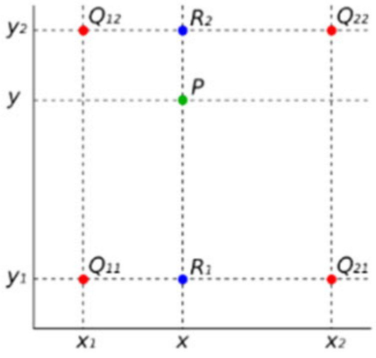

FIGURE 15. Variables of bilinear interpolation.

After the interpolation is completed, diameter change information is incorporated into the image by the following formula:

$$x_{i,j}^{\text{mid}} = n \cdot x_{i,j} \quad (17)$$

$$x_{i,j}^{\text{final}} = \begin{cases} x_{i,j}^{\text{mid}} - (x_{\max} - 255), & x_{i,j}^{\text{mid}} \geq x_{i,j}^{\text{mid}} - 255 \\ 0, & 0 \leq x_{i,j}^{\text{mid}} < x_{i,j}^{\text{mid}} - 255 \end{cases} \quad (18)$$

After processing with Equations (28) and (29), the pixel value curve for a single row of the image is shown in Figure 18. For example, a 6 mm steel bar with a coefficient of $n = 8.5$ is compared to a 25 mm steel bar with a coefficient of $n = 1$. The red dashed line in Figure 16 represents the binarization threshold (Equation (30)), and the green dashed line indicates the reconstructed steel bar width.

Once the dimensional information is integrated into the image, the edge of the steel bar is clarified by employing the threshold binarization method.

$$x_{\text{binary},i,j} = \begin{cases} 255, & x_{i,j}^{\text{final}} \geq 212 \\ 0, & 0 \leq x_{i,j}^{\text{final}} < 212 \end{cases} \quad (19)$$

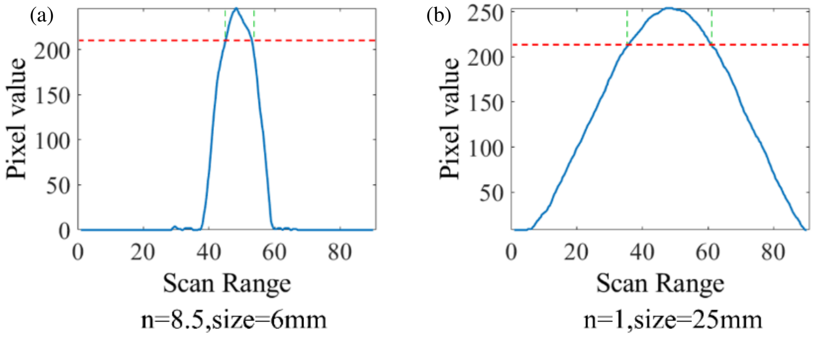

FIGURE 16. Single-row pixel value curves with different coefficients.

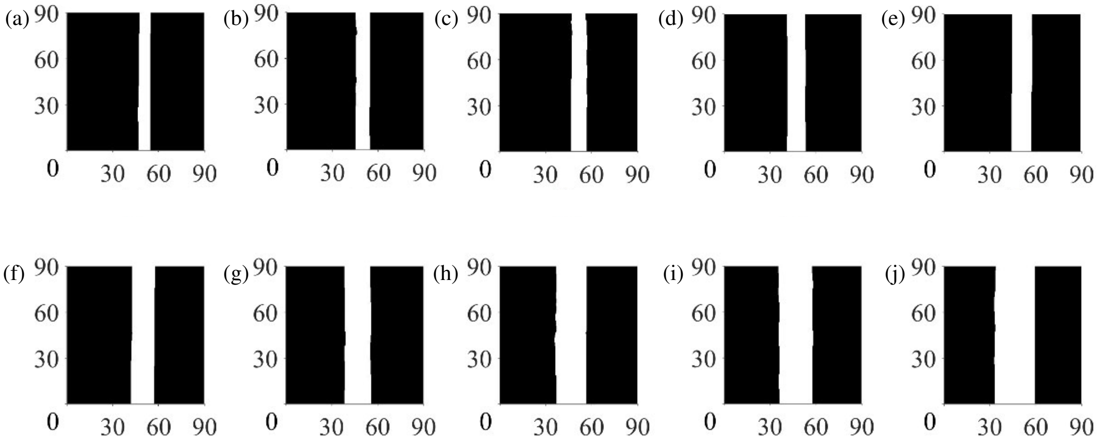

FIGURE 17. Results of imaging reconstruction of vertical steel bars in concrete, the corresponding dimensions are: (a) 6 mm, (b) 8 mm, (c) 10 mm, (d) 12 mm, (e) 14 mm, (f) 16 mm, (g) 18 mm, (h) 20 mm, (i) 22 mm, (j) 25 mm.

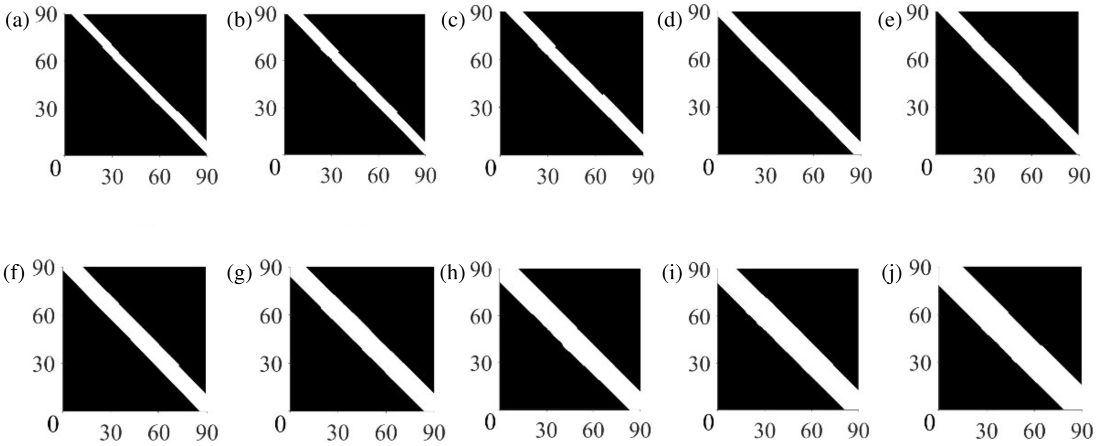

FIGURE 18. 45° oblique rebar image reconstruction results, the corresponding dimensions are: (a) 6 mm, (b) 8 mm, (c) 10 mm, (d) 12 mm, (e) 14 mm, (f) 16 mm, (g) 18 mm, (h) 20 mm, (i) 22 mm, (j) 25 mm.

After being processed by the aforementioned method, the penetrating imaging of steel bars containing dimensional information is presented in Figure 17, Figure 18, and Figure 19.

The accuracy of size recognition and image reconstruction is evaluated using voltage differences for steel bars (6 mm–25 mm) as baselines. White pixel counts in each row of the reconstructed binary image are compared to the total pixel width to assess image width accuracy. Results are presented in Table 6.

The reconstructed images and accuracy results clearly reveal the angle and diameter of the rebars in concrete. This visualization effectively addresses the challenges of on-site detection, where identifying and marking internal rebar structures is difficult. The clear images improve the ability to assess rebar orien-

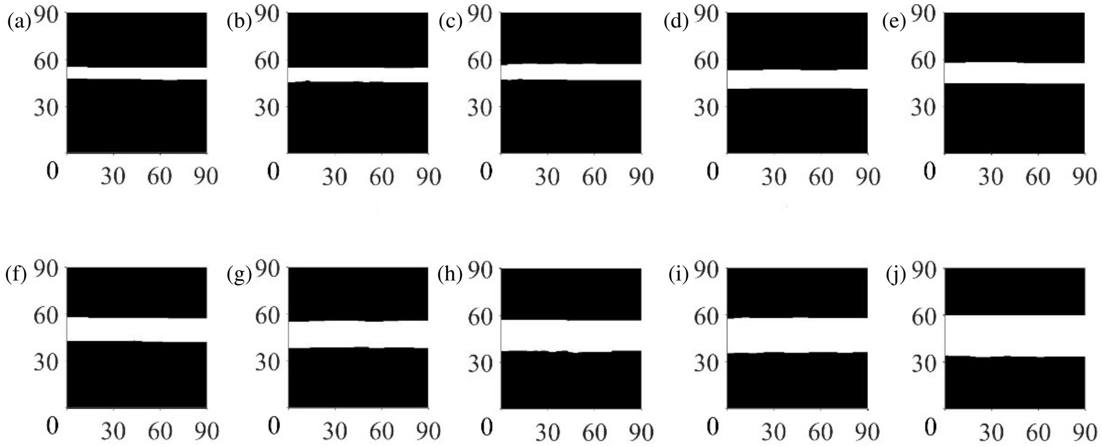

FIGURE 19. Horizontal rebar image reconstruction results, the corresponding dimensions are: (a) 6 mm, (b) 8 mm, (c) 10 mm, (d) 12 mm, (e) 14 mm, (f) 16 mm, (g) 18 mm, (h) 20 mm, (i) 22 mm, (j) 25 mm.

TABLE 6. Accuracy of diameter recognition and image reconstruction.

Diameter (mm)	6	8	10	12	14	16	18	20	22	25
Voltage value	1.7516	1.7496	1.7483	1.7471	1.7453	1.7434	1.7413	1.7407	1.7394	1.7378
Voltage value identified	1.7509	1.7499	1.7487	1.7476	1.7448	1.743	1.7419	1.741	1.7389	1.7374
Diameter recognition accuracy	95.7%	98%	97.2%	96.4%	96.4%	97.2%	95.7%	97.9%	96.4%	97.2%
Ideal pixel width	17	23	28	34	40	45	51	57	63	71
Actual pixel width	18	21	29	32	39	45	52	56	61	73
Reconstruction accuracy	94.2%	91.3%	96.5%	94.2%	97.5%	100%	98.1%	98.3%	96.9%	97.2%

tation and dimensions, overcoming the limitations of traditional nondestructive testing methods.

5. CONCLUSION

This paper introduces a deep learning approach using magnetic resonance eddy current detection for rebar analysis. It involves three steps: (1) acquiring and preprocessing voltage matrix data, (2) extracting the central axis with Skel-Unet, and (3) reconstructing rebar images using thresholds. Voltage data is collected from meshed regions and processed to generate rebar images. Skel-Unet accurately extracts the central axis, enabling rebar orientation and size determination based on peak and valley voltages. The binarization method defines boundaries for size discrimination. This approach enhances rebar identification and calibration, offering significant potential for nondestructive testing in civil engineering.

ACKNOWLEDGEMENT

This study was supported by the National Natural Science Foundation of China (52278146), the Natural Science Foundation of Chongqing, China (CSTB2023NSCQ-LZX0062).

REFERENCES

[1] Hu, J. Y., S. S. Zhang, E. Chen, and W. G. Li, "A review on corrosion detection and protection of existing reinforced concrete (RC) structures," *Construction and Building Materials*, Vol. 325, 126718, 2022.

[2] Han, X., G. Li, P. Wang, Z. Chen, D. Cui, H. Zhang, L. Tian, X. Zhou, Z. Jin, and T. Zhao, "A new method and device for detecting rebars in concrete based on capacitance," *Measurement*, Vol. 202, 111721, 2022.

[3] Goffin, B., N. Banthia, and N. Yonemitsu, "Use of infrared thermal imaging to detect corrosion of epoxy coated and uncoated rebar in concrete," *Construction and Building Materials*, Vol. 263, 120162, 2020.

[4] Chen, R., K. T. Tran, H. M. La, T. Rawlinson, and K. Dinh, "Detection of delamination and rebar debonding in concrete structures with ultrasonic SH-waveform tomography," *Automation in Construction*, Vol. 133, 104004, 2022.

[5] Ham, S. and J. S. Popovics, "Application of contactless ultrasound toward automated inspection of concrete structures," *Automation in Construction*, Vol. 58, 155–164, 2015.

[6] Ichi, E. and S. Dorafshan, "Effectiveness of infrared thermography for delamination detection in reinforced concrete bridge decks," *Automation in Construction*, Vol. 142, 104523, 2022.

[7] Hwang, S., H. Kim, H. J. Lim, P. Liu, and H. Sohn, "Automated visualization of steel structure coating thickness using line laser scanning thermography," *Automation in Construction*, Vol. 139, 104267, 2022.

[8] Ghosh, R., M. Lahoti, and B. Shah, "A succinct review on the use of NMR spectroscopy in monitoring hydration, strength development, and inspection of concrete," *Materials Today: Proceedings*, Vol. 61, 167–173, 2022.

[9] Rubinacci, G., A. Tamburrino, and S. Ventre, "Concrete rebars inspection by eddy current testing," *International Journal of Applied Electromagnetics and Mechanics*, Vol. 25, No. 1-4, 333–

339, 2007.

[10] Pozzer, S., M. P. V. D. Souza, B. Hena, S. Hesam, R. K. Rezayiye, E. R. Azar, F. Lopez, and X. Maldague, "Effect of different imaging modalities on the performance of a CNN: An experimental study on damage segmentation in infrared, visible, and fused images of concrete structures," *NDT & E International*, Vol. 132, 102709, 2022.

[11] Kasai, N., K. Sekino, S. Miyazaki, *et al.*, "An eddy current convergence probe with copper core and single detection coil to detect flaws on aluminum plates," *NDT & E International*, Vol. 132, 102707, 2022.

[12] Chen, H., L. Liao, J. Zhou, H. Zhang, S. Zhang, T. Lan, Z. Zhang, and C. Hu, "Magnetic resonance eddy penetrating imaging for detecting reinforcement corrosion in concrete," *Automation in Construction*, Vol. 165, 105512, 2024.

[13] Li, X., H. Liu, F. Zhou, Z. Chen, I. Giannakis, and E. Slob, "Deep learning-based nondestructive evaluation of reinforcement bars using ground-penetrating radar and electromagnetic induction data," *Computer-Aided Civil and Infrastructure Engineering*, Vol. 37, No. 14, 1834–1853, 2022.

[14] Feng, C.-Q., B.-L. Li, Y.-F. Liu, F. Zhang, Y. Yue, and J.-S. Fan, "Crack assessment using multi-sensor fusion simultaneous localization and mapping (SLAM) and image super-resolution for bridge inspection," *Automation in Construction*, Vol. 155, 105047, 2023.

[15] Wang, X., H. Liu, X. Meng, J. Cui, and Y. Du, "Enhanced imaging of concealed defects behind concrete linings using Residual Channel attention network for rebar clutter suppression," *Automation in Construction*, Vol. 166, 105574, 2024.

[16] Jeon, D., M. K. Kim, Y. Jeong, J. E. Oh, J. Moon, D. J. Kim, and S. Yoon, "High-accuracy rebar position detection using deep learning-based frequency-difference electrical resistance tomography," *Automation in Construction*, Vol. 135, 104116, 2022.

[17] Wang, Z., J. Wang, K. Chen, Z. Li, J. Xu, Y. Li, and Q. Sui, "Unsupervised learning method for rebar signal suppression and defect signal reconstruction and detection in ground penetrating radar images," *Measurement*, Vol. 211, 112652, 2023.

[18] Nguyen, N. H., "U-net based skeletonization and bag of tricks," in *Proceedings of the IEEE/CVF International Conference on Computer Vision (ICCV)*, 2105–2109, Montreal, BC, Canada, Oct. 2021.

[19] Kim, K.-H., P.-S. Shim, and S. Shin, "An alternative bilinear interpolation method between spherical grids," *Atmosphere*, Vol. 10, No. 3, 123, 2019.

[20] Cordonnier, J.-B., A. Loukas, and M. Jaggi, "Multi-head attention: Collaborate instead of concatenate," *arXiv preprint arXiv:2006.16362*, 2020.

[21] Woo, S., J. Park, J.-Y. Lee, and I. S. Kweon, "CBAM: Convolutional block attention module," in *Proceedings of the European Conference on Computer Vision (ECCV)*, 3–19, Munich, Germany, Sep. 2018.

[22] Qin, R., K. Qiao, L. Wang, L. Zeng, J. Chen, and B. Yan, "Weighted focal loss: An effective loss function to overcome unbalance problem of chest X-ray14," in *IOP Conference Series: Materials Science and Engineering*, Vol. 428, No. 1, 012022, Chengdu, China, Jul. 2018.

[23] Zhao, R., B. Qian, X. Zhang, Y. Li, R. Wei, Y. Liu, and Y. Pan, "Rethinking dice loss for medical image segmentation," in *2020 IEEE International Conference on Data Mining (ICDM)*, 851–860, Sorrento, Italy, Nov. 2020.

[24] Liebel, L. and M. Körner, "Auxiliary tasks in multi-task learning," *arXiv preprint arXiv:1805.06334*, 2018.

[25] Lu, X., J. Yao, K. Li, and L. Li, "Cannylines: A parameter-free line segment detector," in *2015 IEEE International Conference on Image Processing (ICIP)*, 507–511, Quebec City, QC, Canada, Sep. 2015.

[26] Ronneberger, O., P. Fischer, and T. Brox, "U-Net: Convolutional networks for biomedical image segmentation," in *Medical Image Computing and Computer-Assisted Intervention — MICCAI 2015*, 234–241, Munich, Germany, Oct. 2015.